Electronic Supplementary Material (ESI) for ChemComm.

Supplementary Information

A computationally-guided non-equilibrium synthesis approach to materials discovery in the SrO-Al_2O_3-SiO_2 phase field

Euan M. Duncan,[a] Amandine Ridouard,[a] Franck Fayon,[a] Emmanuel Veron,[a] Cécile Genevois,[a] Mathieu Allix,[a] Christopher M. Collins,*[b] and Michael J. Pitcher*[a]

[a]*CEMHTI, CNRS UPR3079, 1d Ave. de la Recherche Scientifique, 45071 Orléans, France.*
[b]Department of Chemistry, Materials Innovation Factory, University of Liverpool, Liverpool L7 3NY, U.K.

Contents

A. Methods

Probe Structure Calculations

Probe structures[1] were generated using the Flexible Unit Structure Engine (FUSE version 1.2)[2,3] for 42 compositions (Table S1) in the $SrO - Al_2O_3 - SiO_2$ phase field. For each composition FUSE was run three times, for each run an initial population of 50 random structures was used and the Monte-Carlo search was run until 10,000 structures had been generated since the lowest energy structure was located, with the search divided into generations of five structures, resulting in a total of 1,840,314 structures across the phase field. During the FUSE runs, the General Utility Lattice Program (GULP)[4] was used to perform a local geometry optimisation to obtain their energy using Buckingham interatomic potentials for short ranger interactions (see Table A1, below), with a cut off distance set to 12 Å. The unit cell parameters and atomic positions for each structure were relaxed until the norm of the gradient was less than 0.001 (a.u.). Once all of the FUSE runs had completed, the three lowest energy structures were re-optimised using Density Functional Theory (DFT) using the Vienna Ab-initio Simulation Package (VASP)[5], using the PBE[6] functional and PAW[7] potentials. Both the unit cell and atomic positions were relaxed until the forces were less than 0.02 eV $Å^{-1}$, with a plane wave cutoff energy of 520 eV. K-point grids were generated automatically using VASP's KSPACING function with a parameter set to 0.2. The resulting probe structures were then combined with the structures of ordered known materials and the convex hull; the surface of possible formation energies in the phase field. Formally, a stable composition is said to be on the hull with an energy of 0 meV/atom. Previously, stable oxide phases have been located within ~ 35meV/atom[1,2] and metastable phases within ~65 meV/atom.[8] The hull was calculated using pymatgen.[9]

Table A1*: Parameters used in this work for Buckingham interatomic potentials with GULP, where potential parameters are listed as "Fitted for this work", parameters were fitted using the automatic fitting routine in GULP, and then tested by running FUSE on the corresponding binary oxide, with the parameters re-fitted by hand if necessary to ensure that the lowest energy found using FUSE corresponds to the experimental ground state for each binary material. The fitting for this system has been performed due to the non-transferrable nature of classical interatomic potentials.*

Interaction	A (eV)	rho (Å)	C (eV $Å^{-6}$)	Source
O - O	1388.7700	0.362620	175.00000	As published[10]
O - Al	3028.5814	0.255728	0.087	Fitted for this work, starting from[11]
O – Si	2800.1721	0.254029	10.421304	Fitted for this work, starting from[12]
O - Sr	2077.3751	0.333333	20.474266	Fitted for this work, starting from[13]

Synthesis Procedures

All samples were synthesised by a two-stage glass crystallisation route. All compositions were synthesised from $SrCO_3$ (STREM, 99.995%), SiO_2 (Alfa Aesar, 99.999%) and Al_2O_3 (STREM, 99.98%) powders which were mixed with ethanol and ground by hand in an agate mortar until dry. These mixtures were then pelletised by uniaxial pressing (13mm diameter, 1mm thickness) and broken into ~30mg fragments. Individual fragments were loaded into the nozzle of an aerodynamic levitator system, and melted using a pair of CO_2 lasers, with argon used as the levitation gas. As soon as a stable levitating melt was obtained, the lasers were shut off, allowing the sample to cool rapidly to produce a transparent glass bead. The bead was then crushed, with the resulting glass powder loaded into a platinum crucible and heated in a muffle furnace for 1 hour at a crystallisation temperature determined by in situ PXRD and DSC (typically 850 – 1050 °C, see Figure S4).

Conventional melt-quenching was used to scale up $Sr_{0.344}Al_{0.033}Si_{0.623}O_{1.64}$ glass to the ~5g scale for neutron diffraction, and also for the synthesis of 0.40 SrO – 0.60 SiO_2 glass. Instead of using containerless aerodynamic levitation for precursor glass synthesis, the powdered reaction mixture was loaded into a platinum crucible, then melted in a muffle furnace at 1650°C and allowed to equilibrate for 1 hour. The crucible was then quenched by removing it from the furnace and placing it immediately into cold water. The resulting precursor glass was then ground into powder using an agate mortar, and re-loaded into the platinum crucible prior to the crystallisation step (carried out in the same way as for ADL-prepared glasses).

Powder Diffraction

Ambient temperature laboratory PXRD was conducted in Bragg-Brentano geometry on a Bruker D8 Advance diffractometer with a LynxEye XE detector, using Cu $K\alpha_{1,2}$ incident radiation. Samples were dispersed on a silicon wafer using an ethanol mull. High temperature PXRD was conducted at up to 1200°C in air using an Anton Paar HTK12 furnace, installed on a Bruker D8 Advance diffractometer with a Vantec detector. Samples were loaded in a platinum-lined alumina holder and measured in Bragg-Brentano geometry. High resolution synchrotron PXRD was conducted at ambient temperature on the 11BM beamline (Argonne National Laboratory, U. S. A.). The sample was contained in 0.8mm Kapton capillaries and spun during the measurement at an incident wavelength of 0.458084 Å. Neutron powder diffraction data were collected at ambient temperature at the D2B beamline (Institut Laue Langevin, France, 10.5291/ILL-DATA.EASY-745) with an incident wavelength of 1.5936 Å. The sample was contained in a thin walled vanadium can of 8mm diameter. Pattern indexing, structure solution and Rietveld refinement were conducted Topas Academic v6.[14]

Transmission Electron Microscopy

Imaging, electron diffraction and EDS analysis were conducted using a JEOL ARM200 Cold FEG double corrected with a voltage/current of 200 kV / 13 µA. Samples were prepared by depositing finely ground powders preliminary dispersed in ethanol onto a copper grid coated with a holey amorphous carbon layer. Compositions close to $Sr_2Si_3O_8$ were found to be very susceptible to damage from the incident electron beam, and this proved to be a severe limitation for detailed TEM analysis. Beam current, beam intensity and sample exposure times were therefore minimised during the experiments. EDS analyses were carried out in TEM mode with a condenser aperture of 10 µm: single data points are reported

here (Table S5), due to the difficulty in locating fully-resolved crystalline and glassy regions, and the sample instability.

MAS-NMR

The ^{29}Si magic angle spinning (MAS) NMR experiments were conducted on a Bruker Avance III spectrometer operating at a magnetic field of 9.4 T (^{29}Si Larmor frequency of 79.4 MHz) with a 4mm probehead. ^{29}Si quantitative MAS spectra were recorded at spinning frequencies of 10 and 2 kHz using 1 µs pulse duration (15° flip angle) and a recycling delay of 75 s. 2048 up to 4096 transients were co-added. ^{29}Si chemical shifts were referenced relative to TMS at 0 ppm. ^{29}Si isotropic and anisotropic chemical shift parameters were obtained from fits of experimental spectra using the Dmfit software.[15] Computations of NMR chemical shielding were done with the GIPAW method,[16] using the CASTEP code,[17] PBE functional[6] and ultrasoft pseudopotential[18] (Materials Studio 20.0) generated on-the-fly. The plane wave cutoff energy was set to 600 eV and the k-point grid was sampled with a spacing of 0.04 A^{-1}. Atomic positions were relaxed until forces were less than 0.01 $eV.A^{-1}$, while fixing cell parameters to experimental values with $P2_1/c$ symmetry. Calculated ^{29}Si isotropic shielding values were converted into ^{29}Si isotropic chemical shift using the following relationship established using reference compounds: $\delta_{iso}=0.939\sigma_{iso} + 300.5$.

Thermal Analysis

Glass crystallisation temperatures were evaluated using a Setaram MULTI HTC 1600 differential scanning calorimeter, from powder samples contained in a platinum vessel. Measurements were run in an argon atmosphere at a heating rate of $10°min^{-1}$.

B. Supplementary Figures (S1 – S12)

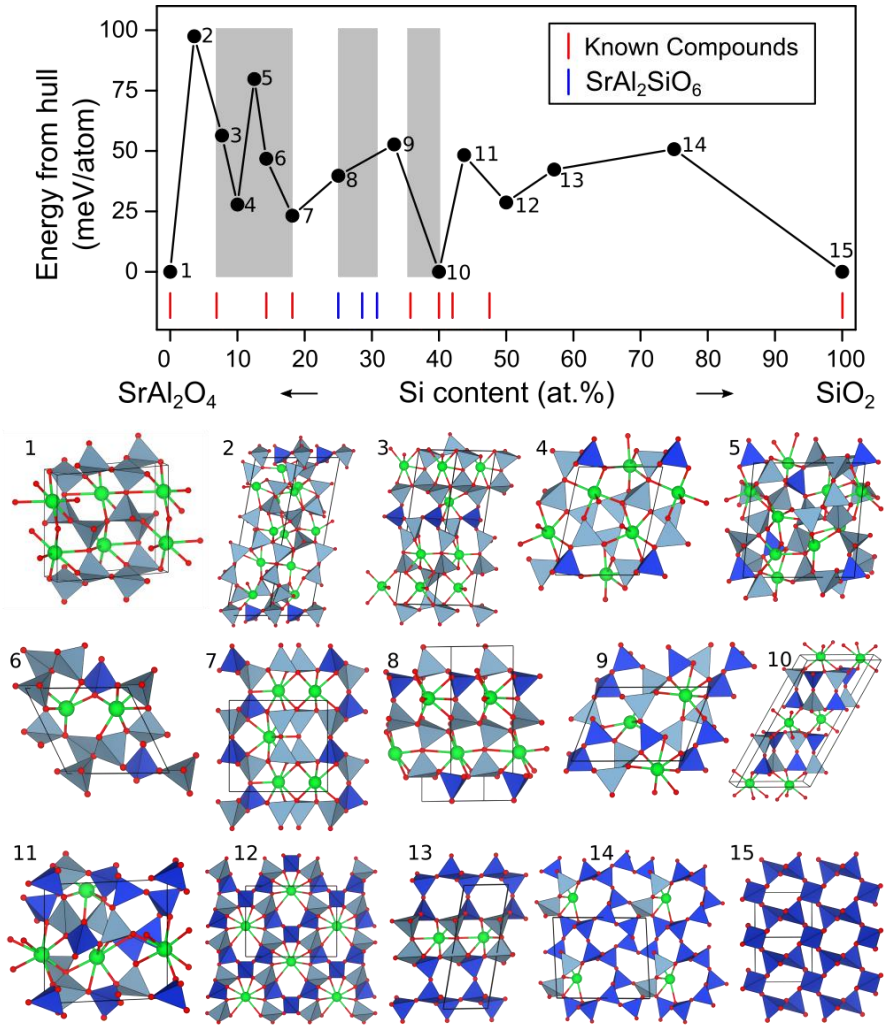

Figure S1*. Probe structure calculations for compositions along the tie line $SrAl_2O_4$ – SiO_2. (a) Energies obtained from 15 points across the compositional range, with red markers indicating known crystalline compounds and blue markers corresponding to metastable $SrAl_2SiO_6$. Shaded regions correspond to the $SrAl_2O_4$-, $SrAl_2SiO_6$- and $SrAl_2Si_2O_8$-structural domains that can be accessed by glass crystallisation.[19] (b) Projections of the probe structures calculated for each point using FUSE, which all consist of corner-sharing tetrahedral $(Al/Si)O_4$-frameworks.*

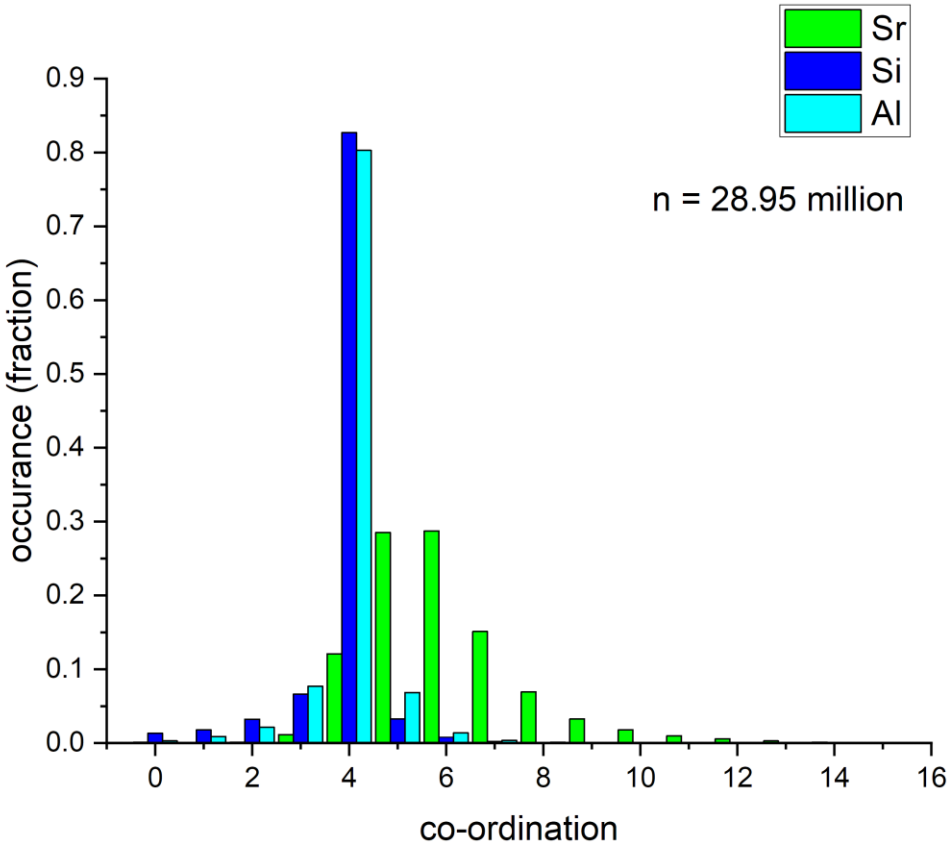

Figure S2*. Local coordination numbers of Sr, Si and Al collated from all of the FUSE-generated structures (total of 2.895 x 10^7 coordination environments) using previously-defined bond distance cutoffs,[1] shown here to illustrate the range of co-ordination environments accessible by FUSE.*

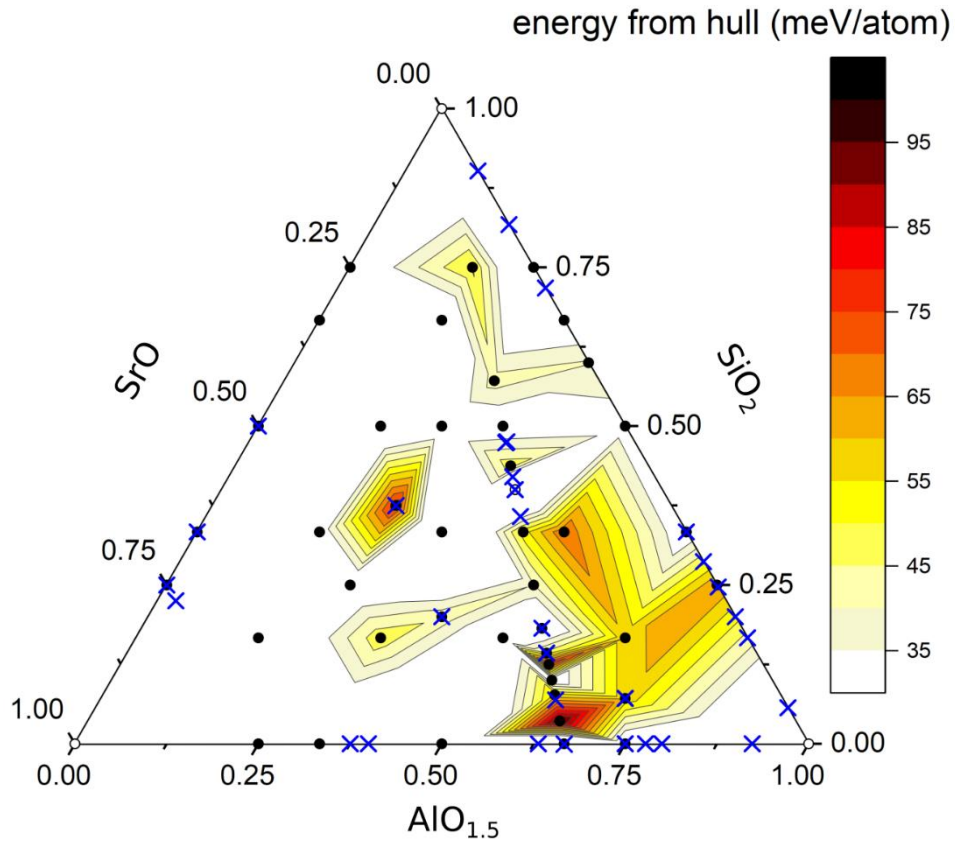

Figure S3*. The calculated convex hull from Figure 1 (main text), displayed here with a 35 meV/atom cutoff.*

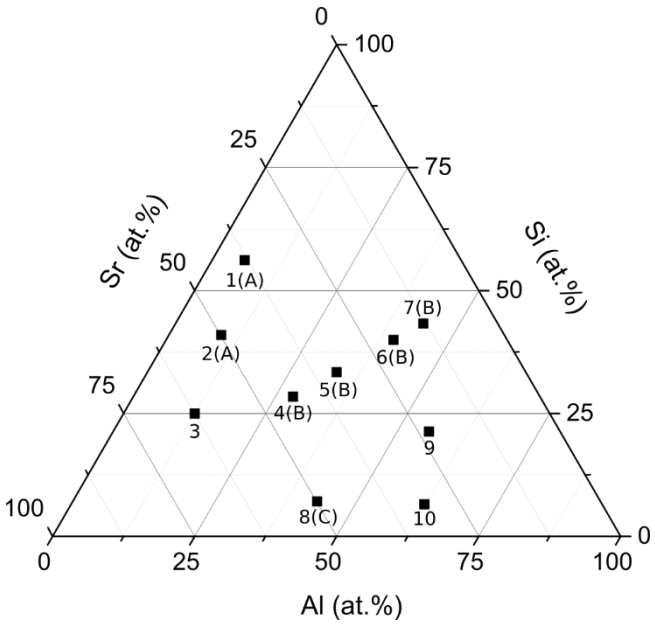

	T_{quench} / °C	$T_{cryst.}$ / °C
1(A)	1480	900
2(A)	1720	850
3	2300	-
4(B)	1650	925
5(B)	1650	1050
6(B)*	1700	1020
7(B)	1650	1000
8(C)	1800	900
9	1650	1000
10†	1900	951

*From Al Saghir *et. al.*, *Chem. Mater.* 27(2), 508-514 (2015)

†From Fernandez-Carrion *et. al., Inorg. Chem.* 56(23), 14446-14458 (2017)

***Figure S4**. Glass quench temperatures and crystallisation temperatures determined for representative compositions within (or close to) regions **A, B** and **C**. Quenching temperatures (T_{quench}) were obtained from pyrometer readings of levitating melts, taken just before laser shut-off. Crystallisation temperatures ($T_{cryst.}$) were obtained by in-situ PXRD on heating in steps of either 25 or 50°C (range 600 – 1200°C). Two data points from the literature (**6(B)** and **10**) have also been included for completeness. Note that composition **3** melted but did not form glass on quenching.*

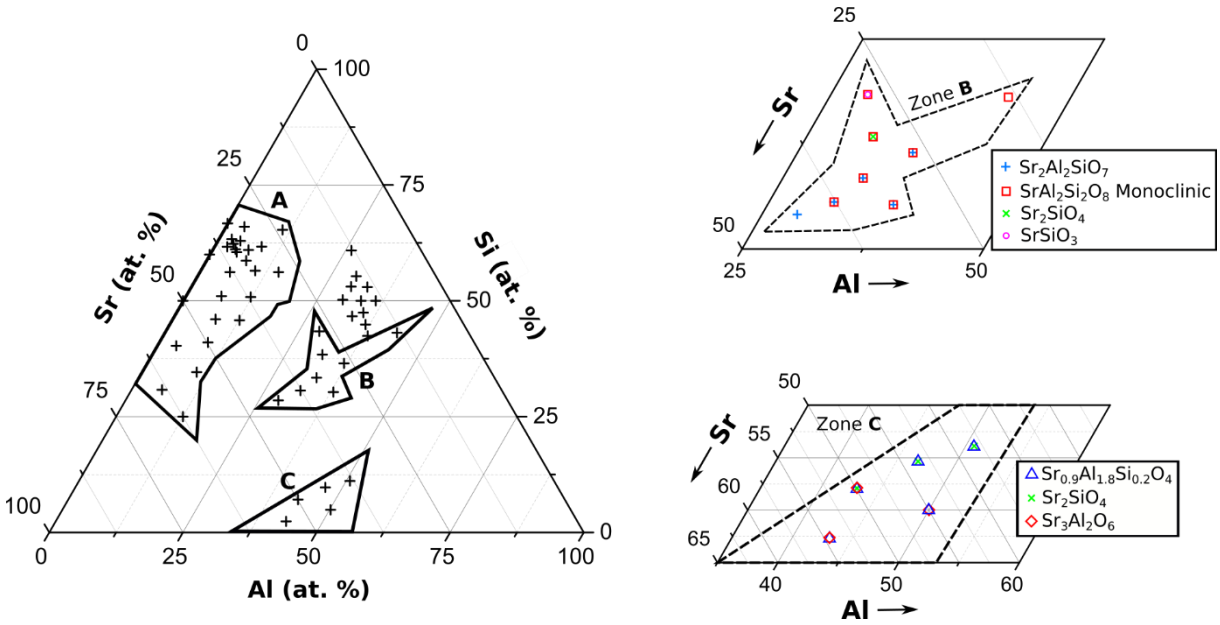

Figure S5*. Compositions explored by glass crystallisation synthesis (see Figure X of the main manuscript for calculated hull), marked by black crosses. The results from Zone A are presented in the main manuscript. Zones B and C, shown here, only yielded mixtures of known phases, as summarised in the legends. Additional compositions were explored close to the $SrAl_2O_4$ – SiO_2 tie line (see data points grouped between Zones A and B), and these also yielded mixtures of known phases (principally monoclinic $SrAl_2Si_2O_8$).*

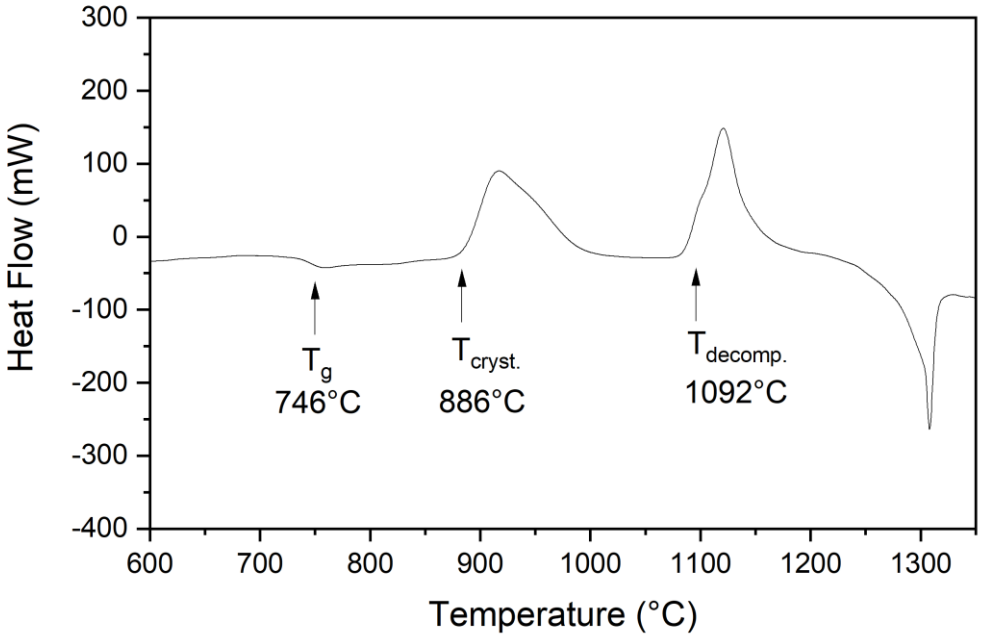

***Figure S6**: DSC scan of $Sr_{0.344}Al_{0.033}Si_{0.623}O_{1.64}$ glass measured on heating at 10°C min^{-1} from ambient temperature through its melting point (sample mass 630 mg, platinum container, argon gas flow). The material undergoes a glass transition (T_g), then crystallises into $Sr_2Si_3O_8$ ($T_{cryst.}$), which then decomposes into crystalline $SrSiO_3$ + amorphous aluminosilicate ($T_{decomp.}$) before melting at ~1300°C.*

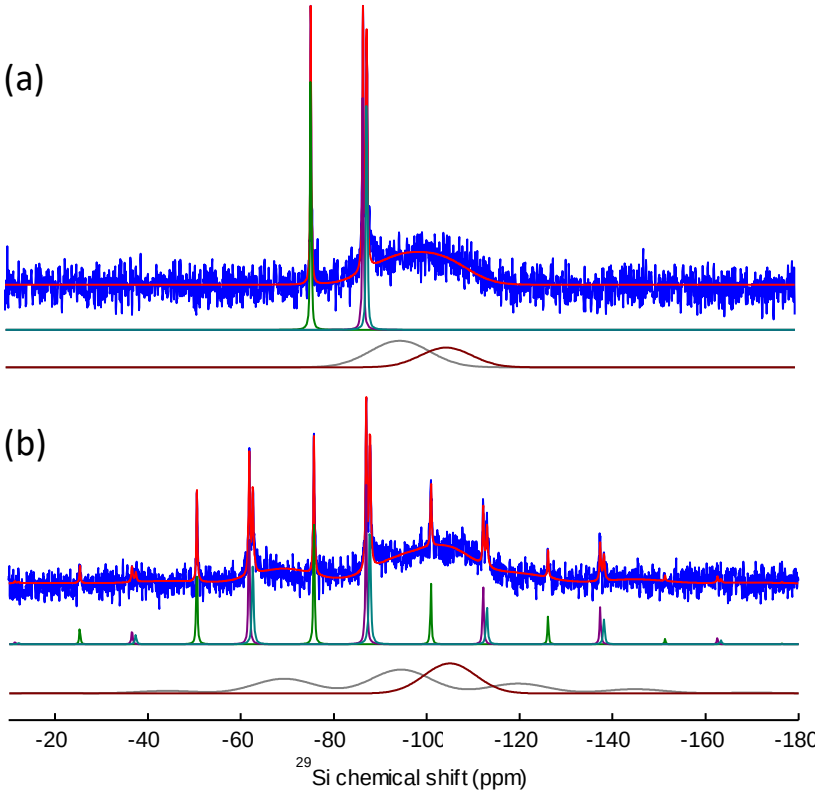

***Figure S7**: Experimental ^{29}Si MAS NMR spectra of crystallised $Sr_{0.344}Al_{0.033}Si_{0.623}O_{1.64}$ (blue) recorded at spinning rates of (a) 10 and (b) 2 kHz, and their simulations (red line). The three narrow peaks corresponding to the crystalline $Sr_2Si_3O_8$ phase and the two broad lines associated to the residual glass phase (grey and brown) are shown below the experimental spectra.*

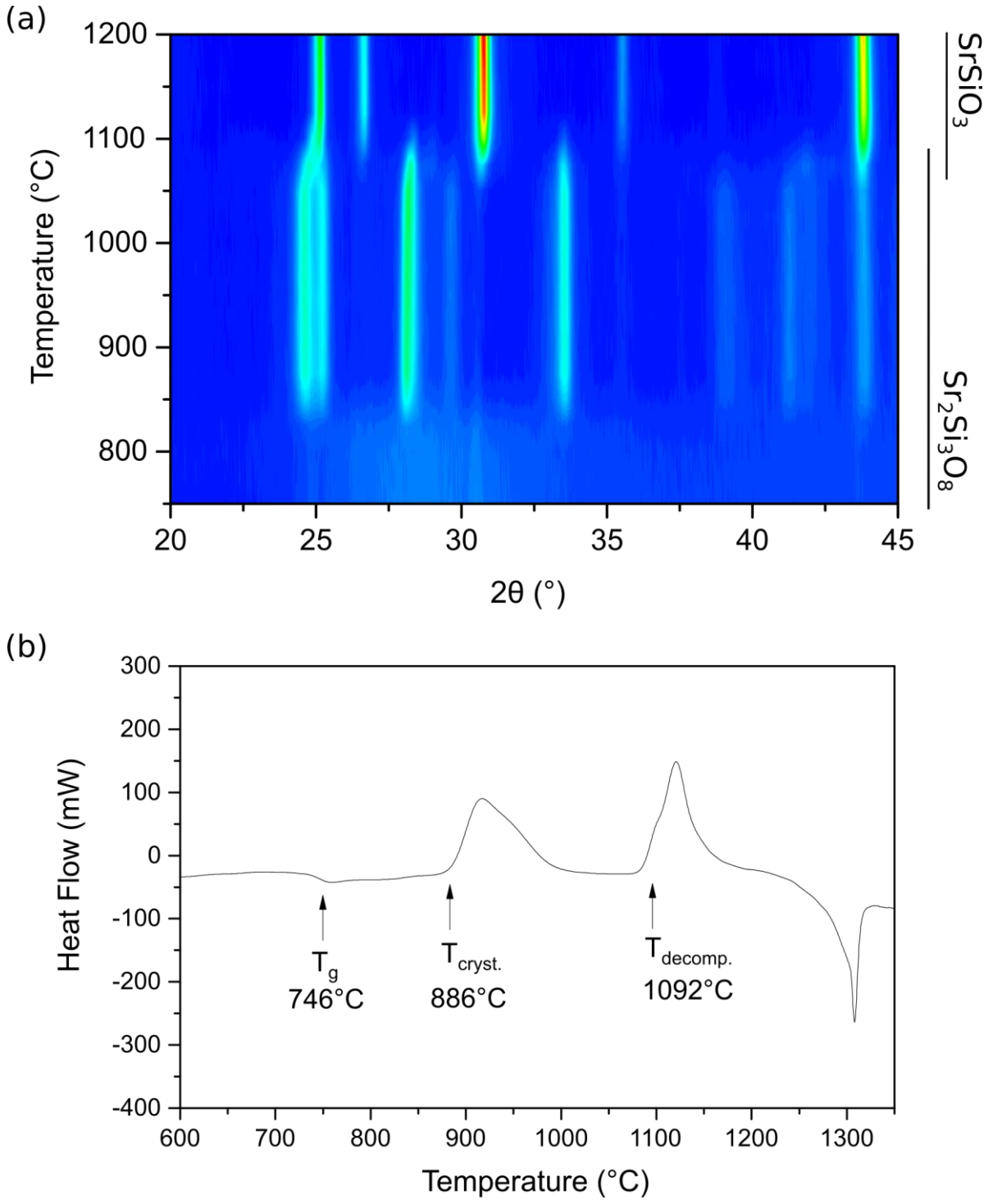

Figure S8*. (a) In-situ PXRD of the same precursor glass, collected on heating, showing crystallisation of $Sr_2Si_3O_8$ at ~825°C, which is then retained as the only crystalline phase until thermal decomposition products (crystalline $SrSiO_3$) appear above 1050°C. (b) DSC scan of $Sr_2Si_3O_8$ glass (0.40SrO – 0.60SiO_2) measured on heating at 10°C min^{-1} from ambient temperature through its melting point (sample mass 598 mg, platinum container, argon gas flow). The material undergoes a glass transition (T_g ~750°C), then crystallises into $Sr_2Si_3O_8$ (T_{cryst} ~859°C.), which then decomposes into crystalline $SrSiO_3$ + amorphous silicate (T_{decomp} ~1110°C.) before melting at ~1350°C.*

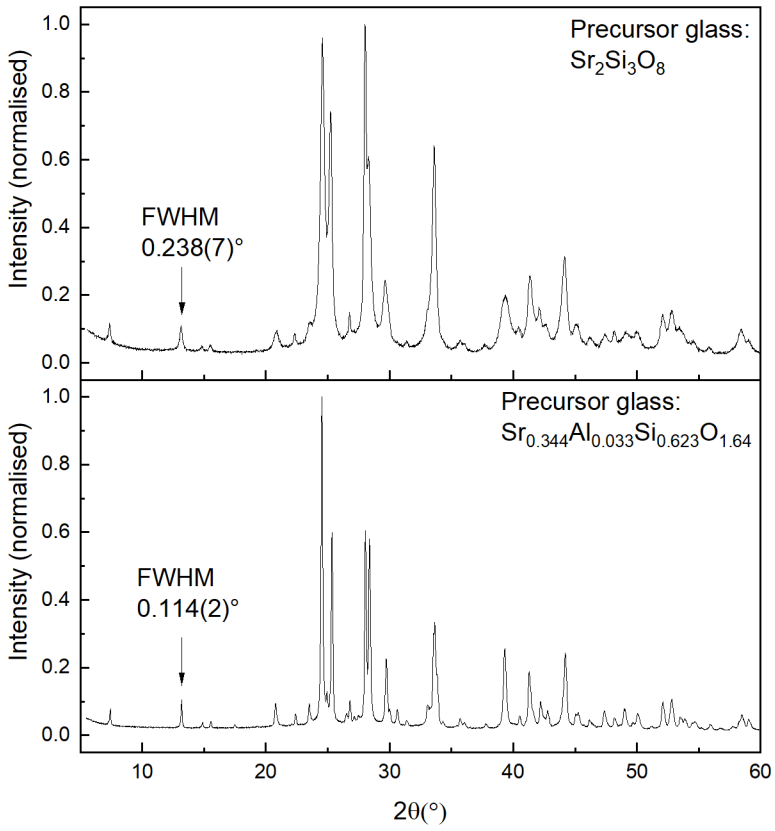

***Figure S9**: Laboratory PXRD patterns of $Sr_2Si_3O_8$ crystallised homogeneously from precursor glass of the same nominal composition ($Sr_2Si_3O_8$, above) or heterogeneously from an alumina-containing glass composition ($Sr_{0.34}Al_{0.033}Si_{0.623}O_{1.64}$, below). Whilst neither sample crystallises fully (both retain a residual amorphous phase), the heterogeneous crystallisation results in a substantially higher crystalline quality, as shown by the difference in peak widths (FWHM) of the two samples.*

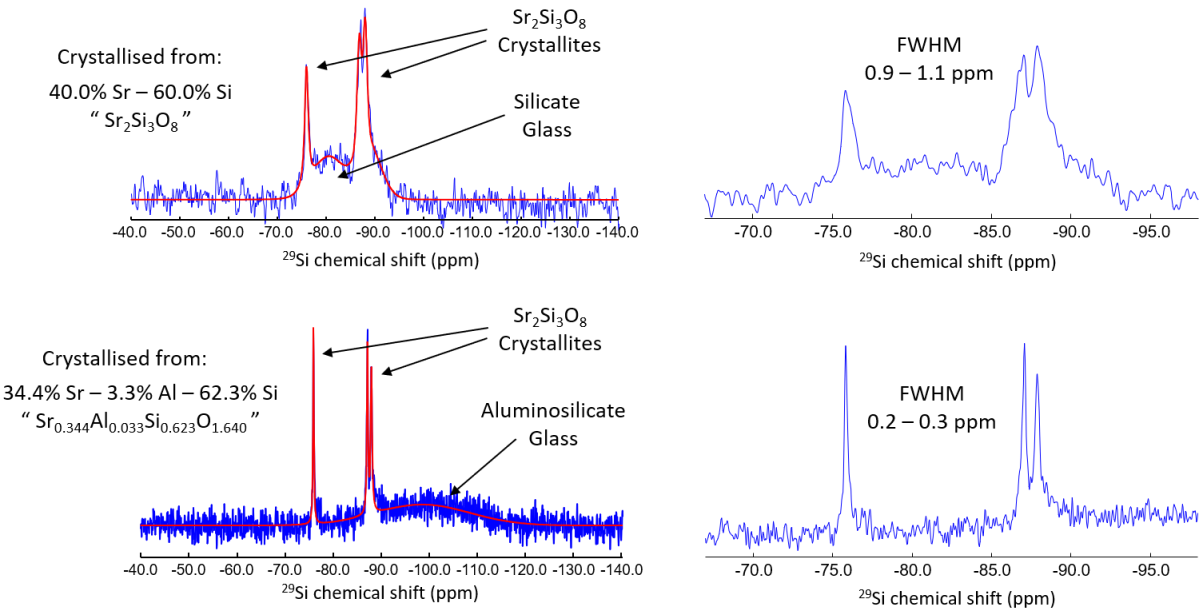

***Figure S10**: Comparison of the ^{29}Si NMR spectra of $Sr_2Si_3O_8$ crystallised from an alumina-containing glass (starting composition $Sr_{0.344}Al_{0.033}Si_{0.623}O_{1.640}$, see main text) or from an alumina-free glass of the correct nominal composition ($Sr_2Si_3O_8$). Both samples retain substantial amorphous phase fractions, but the alumina-free sample also has significantly broader resonances, indicating that the crystalline phase has lower crystallinity when crystallised from glass of the same composition. This is in qualitative agreement with the PXRD analysis of the two samples.*

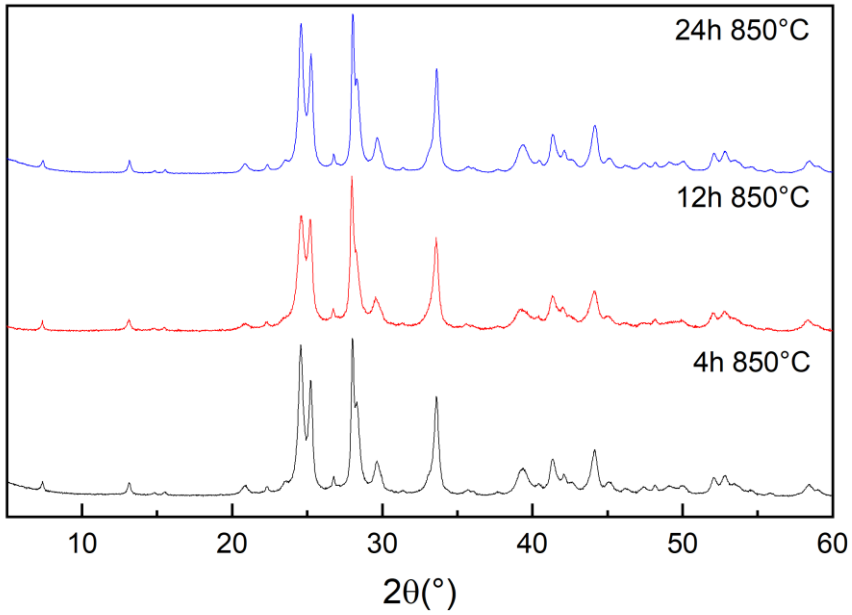

***Figure S11**. PXRDs of $Sr_2Si_3O_8$ crystallised from 0.40 SrO – 0.60 SiO_2 glass powder at 850°C for different times (4 – 24h). Although there is no apparent thermal decomposition of the samples, the extended annealing times do not produce any significant improvement of the crystallinity.*

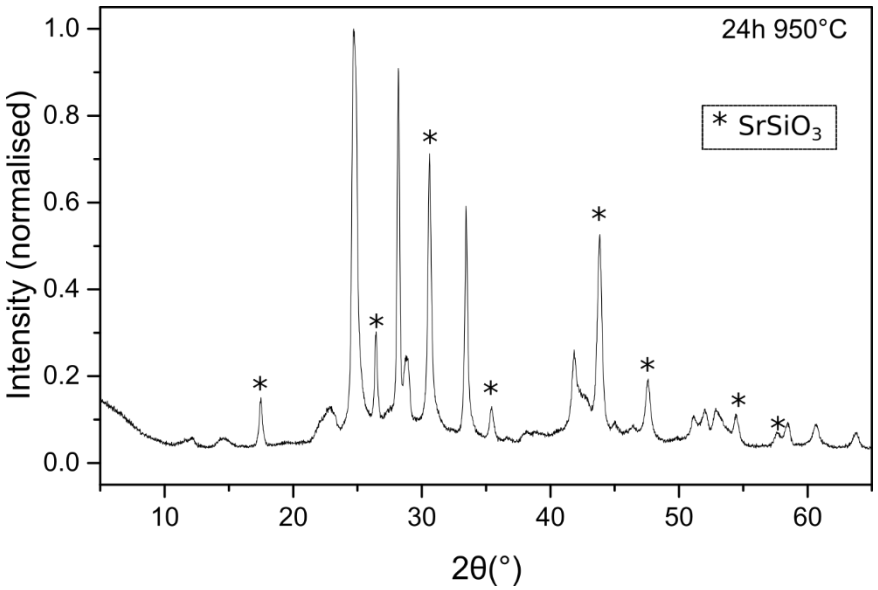

***Figure S12**. PXRDs of $Sr_2Si_3O_8$ crystallised from 0.40 SrO – 0.60 SiO_2 glass powder at 950°C for 24h. The sample contains a substantial amount of the thermal decomposition product $SrSiO_3$ (*).*

C. Supplementary Tables (S1 – S4)

Table S1. *Probe structure compositions and calculated energies used to construct the convex hull (Figure 1 of the main text).*

Probe Structure (Reference #)	Composition (stoichiometry)				E (meV/atom)
	Al	O	Si	Sr	
1	2	15	6	0	11.1681
2	2	9	3	0	40.53777
3	6	13	2	0	64.97997
4	2	5	1	0	28.19468
5	2	11	4	0	27.38549
6	6	11	0	2	25.38144
7	2	5	0	2	0
8	2	9	0	6	21.58641
9	2	4	0	1	0
10	2	7	0	4	16.0729
11	0	7	3	1	26.31483
12	0	3	1	1	0
13	0	5	1	3	0
14	0	5	2	1	16.04519
15	0	4	1	2	0
16	2	21	8	2	22.29619
17	2	10	3	1	28.70023
18	6	19	4	2	69.5677
19	4	9	1	1	58.55174
20	2	13	4	2	26.50456
21	2	6	1	1	39.75958
22	6	17	2	4	22.86801
23	2	9	2	2	0
24	2	19	6	4	17.91119
25	2	8	1	3	48.87679
26	2	11	2	4	25.44788
27	2	17	4	6	29.34849
28	2	15	2	8	16.14112
30	2	22	9	1	50.71492
31	2	12	4	1	42.33299
32	6	26	7	3	48.31591
33	4	14	3	2	52.68104
34	6	16	2	3	23.17993
35	14	34	3	7	79.76642
36	8	18	1	4	56.39702
37	18	38	1	9	97.46505
39	6	14	1	3	27.8395
40	2	8	2	1	0
41	4	10	1	2	46.76193
44	2	7	2	0	30.70462
45	2	7	1	2	43.37948
46	10	20	1	3	58.51218

***Table S2**: Crystal structure of $Sr_2Si_3O_8$ (sample crystallised from precursor glass of nominal composition $Sr_{0.344}Al_{0.033}Si_{0.623}O_{1.640}$), refined against synchrotron XRD data (11BM, λ = 0.458084 Å). This model corresponds to Rietveld the fit displayed in Figure 2(a) of the main manuscript. The corresponding Crystallographic Information File is available from CCDC-FIZ Kahlsruhe (https://www.ccdc.cam.ac.uk/structures/) under deposition number 2266977.*

Atom	*Site*	*x*	*y*	*z*	*Occupancy*	B_{iso} (Å^2)
Sr1	4*e*	0.64289(6)	0.2324(2)	0.59994(6)	1	0.782(16)
Sr2	4*e*	0.08458(6)	0.2155(2)	0.18708(6)	1	0.695(17)
Si1	4*e*	0.13936(17)	0.2124(7)	0.93610(16)	1	0.67(5)
Si2	4*e*	0.78027(16)	0.2245(8)	0.40971(17)	1	0.87(5)
Si3	4*e*	0.52590(19)	0.1797(6)	0.82703(19)	1	0.52(5)
O1	4*e*	0.8676(4)	0.1072(10)	0.0207(3)	1	0.69(4)
O2	4*e*	0.1833(4)	0.1251(11)	0.5566(3)	1	0.69(4)
O3	4*e*	0.0215(3)	0.1942(13)	0.3473(3)	1	0.69(4)
O4	4*e*	0.2342(3)	0.2312(14)	0.8916(3)	1	0.69(4)
O5	4*e*	0.6596(3)	0.2093(13)	0.9110(3)	1	0.69(4)
O6	4*e*	0.7788(3)	0.2034(13)	0.7996(3)	1	0.69(4)
O7	4*e*	0.4610(3)	0.2498(15)	0.3985(3)	1	0.69(4)
O8	4*e*	0.4927(3)	0.1638(12)	0.2092(3)	1	0.69(4)
Space Group		$P2_1/c$				
Z		4				
Lattice Parameters (Å)		*a* = 13.32739(11), *b* = 4.58225(4), *c* = 13.46481(10), γ = 116.6955(3)				
Unit Cell Volume (Å^3)		734.638(11)				
R_{wp} (%)		7.34				
χ^2		1.35				

***Table S3**: Crystal structure of $Sr_2Si_3O_8$ (sample crystallised from precursor glass of nominal composition $Sr_{0.344}Al_{0.033}Si_{0.623}O_{1.640}$), refined against neutron diffraction data (D2B, λ = 1.5936 Å). This model corresponds to the Rietveld fit displayed in Figure 2(b) of the main manuscript.*

Atom	*Site*	*x*	*y*	*z*	*Occupancy*	B_{iso} (Å^2)
Sr1	4*e*	0.6440(3)	0.2214(10)	0.6011(3)	1	0.20(5)
Sr2	4*e*	0.0861(3)	0.2149(11)	0.1878(3)	1	0.20(5)
Si1	4*e*	0.1415(5)	0.2152(14)	0.9373(5)	1	0.22(7)
Si2	4*e*	0.7803(4)	0.2247(17)	0.4098(5)	1	0.22(7)
Si3	4*e*	0.5251(5)	0.1811(17)	0.8270(6)	1	0.22(7)
O1	4*e*	0.8716(4)	0.1183(10)	0.0209(4)	1	0.51(4)
O2	4*e*	0.1804(4)	0.1223(12)	0.5596(4)	1	0.51(4)
O3	4*e*	0.0200(4)	0.1994(12)	0.3445(4)	1	0.51(4)
O4	4*e*	0.2345(4)	0.2435(11)	0.8923(4)	1	0.51(4)
O5	4*e*	0.6612(4)	0.2323(12)	0.9126(4)	1	0.51(4)
O6	4*e*	0.7784(4)	0.2019(12)	0.7963(4)	1	0.51(4)
O7	4*e*	0.4618(4)	0.2485(14)	0.8983(4)	1	0.51(4)
O8	4*e*	0.4940(4)	0.1644(12)	0.2088(4)	1	0.51(4)
Space Group		$P2_1/c$				
Z		4				
Lattice Parameters (Å)		*a* = 13.3249(5), *b* = 4.58044(19), *c* = 13.4626(5), γ = 116.709(2)				
Unit Cell Volume (Å^3)		734.01(5)				
R_{wp} (%)		3.00				
χ^2		1.72				

***Table S4**: ^{29}Si isotropic chemical shifts (δ_{iso}), chemical shift anisotropy parameters (δ_{csa}, η_{csa}) and relative intensities (I) of the 3 inequivalent Si sites of $Sr_2Si_3O_8$ determined from fits of experimental MAS spectra recorded at 9.4T with spinning frequencies of 10 and 2 kHz. The ^{29}Si chemical shielding parameters (σ_{iso}, $\delta_{csa}=-\sigma_{csa}$, η_{csa}) calculated using the GIPAW method for the $Sr_2Si_3O_8$ structural model after DFT relaxation of atomic positions are given in italics. Calculated isotropic shifts are obtained from the relationship $\delta_{iso}=0.939\sigma_{iso}+300.5$.*

Site	Type		δ_{iso} (ppm)	σ_{iso} (ppm)	δ_{csa} (ppm)	η_{csa}	Fwhm (ppm)	I (%)
Si1	Q^2	Exp	-75.9		-60	0.64	0.26	32.2
		GIPAW	*-77.3*	*402.4*	*-63.9*	*0.47*		*33.3*
Si2	Q^3	Exp	-87.9		-60	0.15	0.32	33.7
		GIPAW	*-89.3*	*415.1*	*-65.9*	*0.21*		*33.3*
Si3	Q^3	Exp	-87.1		-62	0.21	0.29	34.1
		GIPAW	*-88.9*	*414.7*	*-72.3*	*0.31*		*33.3*

***Table S5**: TEM-EDS analysis of $Sr_2Si_3O_8$ crystallised from precursor glass of nominal composition $Sr_{0.344}Al_{0.033}Si_{0.623}O_{1.640}$, corresponding to the crystalline and glassy zones of the TEM image shown in Figure 3(a) of the main manuscript. The nominal (parent glass) composition is also tabulated for reference.*

Zone	**Sr (at. %)**	**Si (at. %)**	**Al (at. %)**
Crystalline*	41	59	-
Glass (1)†	32.2	65.2	2.6
Glass (2)†	32.5	65.5	2.0
Mixed‡	37	62	1
Nominal (parent glass)	*34.4*	*62.3*	*3.3*

* *Single EDS spectrum measured from a fully-resolved crystalline region of ~20 nm. The Al EDS signal from this region was below the detection threshold.*

† *Single spectra measured from two different fully-resolved glassy regions of size 20-30 nm*

‡ *Spectrum of a mixed crystalline-glass region of ~300 nm, representing an average composition.*

D. *Ab initio* structure solution of $Sr_2Si_3O_8$

Structure solution was carried out by a simulated annealing approach using synchrotron PXRD data (11BM, λ = 0.458084 Å). First, the pattern was indexed to a monoclinic unit cell of dimensions a = 13.327 Å, b = 4.582 Å, c = 13.464 Å and β = 116.7° using Topas Academic v.6.[20] Candidate space groups $P2_1/c$ and Pc were identified based on systemic absences, and these provided near-identical Pawley fits to the data. The higher symmetry space group $P2_1/c$ was selected for structure solution attempts, due to its smaller asymmetric unit.

With no *a priori* knowledge of the composition of the crystalline phase, the initial simulated annealing runs were set up with compositions close to the nominal stoichiometry $Sr_{0.344}Al_{0.033}Si_{0.623}O_{1.64}$. First, a tetrahedral [$SiO_4$] rigid body was defined with fixed O-Si-O angles (109.47°) and a single refinable Si-O distance (constrained to the range 1.2 – 1.6 Å). A dynamic occupancy correction[21] was then defined, which gradually merges atoms of the same type as they approach each other in real space within a radius of 1 Å. This gives the model the freedom to link rigid tetrahedra by corner-sharing by merging their shared oxygen positions, and also allows the Sr/Si ratio to change (e.g. by superimposing and merging two Sr or two Si atoms). Anti-bump penalties were used to penalise Sr-O and Sr-Si distances of < 2 Å. Finally, the lattice parameters, zero shift, background function and profile function were all fixed according to values obtained by Pawley refinement. Thermal displacement parameters (B_{iso}) were fixed arbitrarily to 1 $Å^2$ for all atoms. Note that Al^{3+} was not defined explicitly during simulated annealing, due to its identical X-ray scattering factor to Si^{4+}: at this stage, the tetrahedral rigid bodies were interpreted as coordination environments that could be populated by either Al or Si.

Simulated annealing was initiated with 2x Sr^{2+} ions and 4x identical [SiO_4] rigid bodies placed at random positions in the asymmetric unit (Sr:Si ratio of 1:2). The annealed parameters were the x,y,z coordinates of each scattering object, the rotation of each rigid body about 3 axes x,y and z, the Si-O distance (common to each rigid body), and a scale factor. The site occupancies, set initially to 1, were controlled via the dynamic occupancy correction. Using the "Auto_T" simulated annealing macro (Topas v.6[14]) this eventually converged to a reasonable fit to the data (R_{wp} = 12.8%, χ^2 = 4.07), featuring a good description of all of the major features of the diffraction pattern. Inspection of the annealed model revealed physically reasonable coordination environments for Sr^{2+}, but that two of the initial [SiO_4] rigid bodies had merged into a single object to leave a Sr:Si ratio of 2:3 (see Figure D1). This structure was then tidied by merging adjacent atoms to leave only fully-occupied Sr, Si(Al) and O sites, and used as a starting model of composition "$Sr_2Si_3O_8$" for Rietveld refinement as described in the main text.

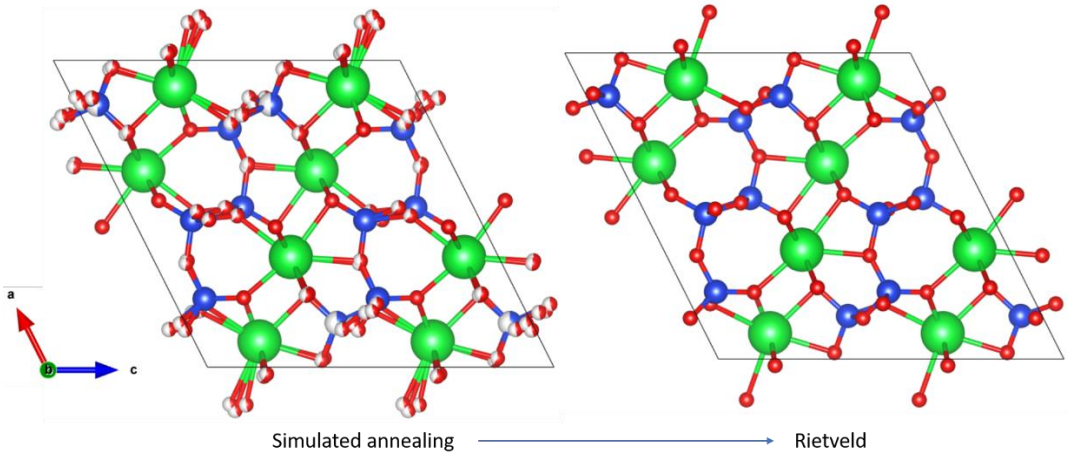

***Figure D1**. The initial structural model obtained by simulated annealing (left), was then tidied to "$Sr_2Si_3O_8$" and used for Rietveld refinement (right).*

E. Comparison of the $Sr_2Si_3O_8$ and $Ba_2Si_3O_8$ Structures

The key differences between the $Sr_2Si_3O_8$ and $Ba_2Si_3O_8$ structures are illustrated in Figures E1 and E2. The $[Si_6O_{16}]^{8-}$ ribbons in $Ba_2Si_3O_8$ have the same topology as those in $Sr_2Si_3O_8$, formed by a row of three $[SiO_4]$ zweier chains which connect to form hexagonal rings of corner-linked tetrahedra with a *ududud* arrangement. In $Ba_2Si_3O_8$, the three diagonals of the hexagonal rings have similar lengths, which lie between 4.67 – 5.15 Å.[22] Starting from these near-regular ribbons, the $Sr_2Si_3O_8$ ribbon is derived by a large cooperative twist of the two external chains, as illustrated by the red arrows in Figure E1. At the same time, the central zweier chain remains essentially unchanged. This distorts the hexagonal *ududud* rings, producing non-equivalent diagonals of length 3.87, 4.58 and 6.06 Å. This is correlated with a major change in the coordination environment of the M^{2+} cation at the ribbon edge ("Sr2" in the crystallographic model), which lies at the interface of three ribbons and coordinates only to their external chains: here, the near-cubic 8-coordinate Ba^{2+} environment is replaced by a more distorted 7-coordinate Sr^{2+} environment in $Sr_2Si_3O_8$. In contrast to Sr2, the 8-coordinate "Sr1" site at the ribbon centre closely resembles that of its Ba counterpart. This site is less affected by the ribbon distortion as it bonds mainly to the central $[SiO_4]$ chain, with no close contacts to either of the oxides associated with the external chain twist ("O1" and "O2"). Whilst the canting angle of the ribbons is similar in the two compounds, the ribbon packing mode changes from a checkerboard-type antiparallel arrangement in $Sr_2Si_3O_8$ to a stripe-type arrangement in $Ba_2Si_3O_8$ (Figure E2). This structural similarity is confirmed by the ^{29}Si MAS-NMR spectra of $Ba_2Si_3O_8$, which exhibits the same 1:1:1 distribution of Q^2 (x1) and Q^3 (x2) sites as that exhibited by $Sr_2Si_3O_8$ (see Figure E3 and Table E1).

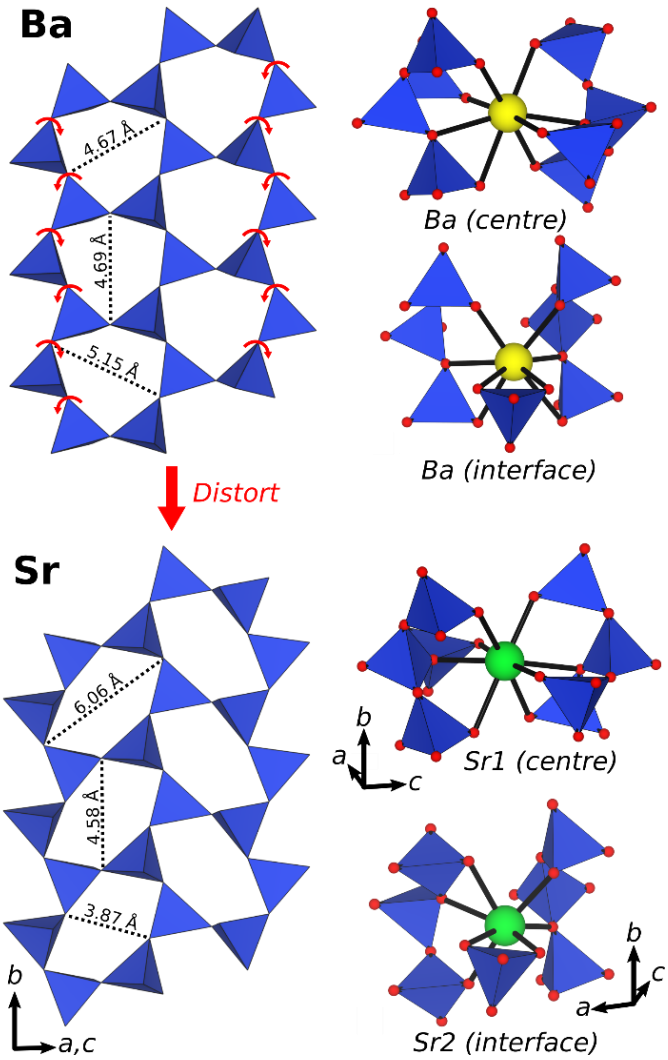

***Figure E1**. Structural comparison of $Ba_2Si_3O_8$ (top, from the work of Hesse and Liebau[22]) and $Sr_2Si_3O_8$ (bottom, this work). Their $[Si_6O_{16}]^{8-}$ ribbons are related by a cooperative twist of the external $[SiO_4]$ chains (red arrows), producing distorted hexagonal rings for $Sr_2Si_3O_8$. The 8-fold coordination environment of Ba (yellow) and Sr (green) at the centre of the ribbons, formed by two neighbouring ribbons from the same stack, is similar in the two structures. The coordination environment at the interface of two stacks, which is formed by bonds to the external $[SiO_4]$ chains of three neighbouring ribbons, is more highly distorted in $Sr_2Si_3O_8$ with Sr in 7-fold coordination, compared to the more symmetrical (near-cubic) 8-fold Ba site in $Ba_2Si_3O_8$.*

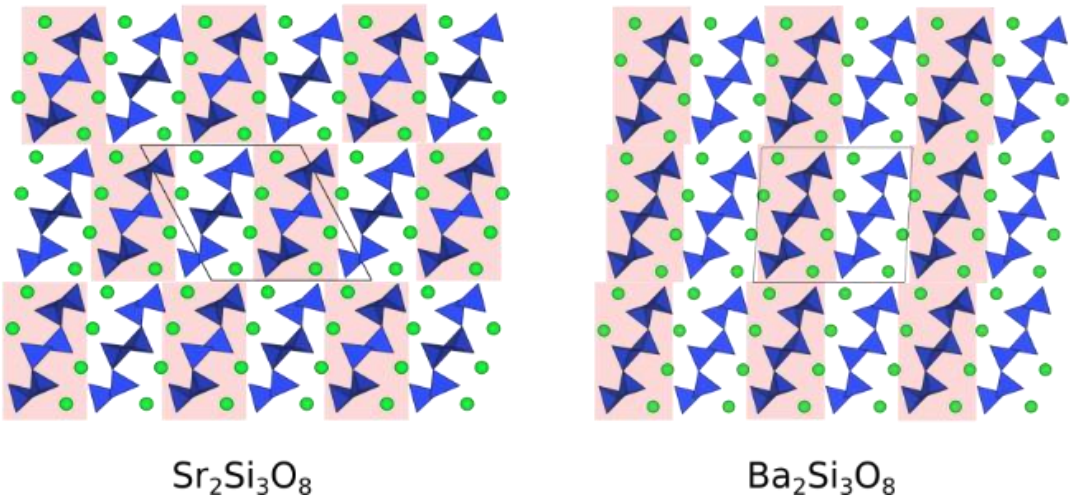

***Figure E2**. Comparison of the $[Si_6O_{16}]^{4-}$ ribbon packing arrangements in $Sr_2Si_3O_8$ and $Ba_2Si_3O_8$. Both structures adopt antiparallel arrangements, which are checkerboard-like in $Sr_2Si_3O_8$ (this work), and stripe-like in $Ba_2Si_3O_8$ (Hesse and Liebau[22]).*

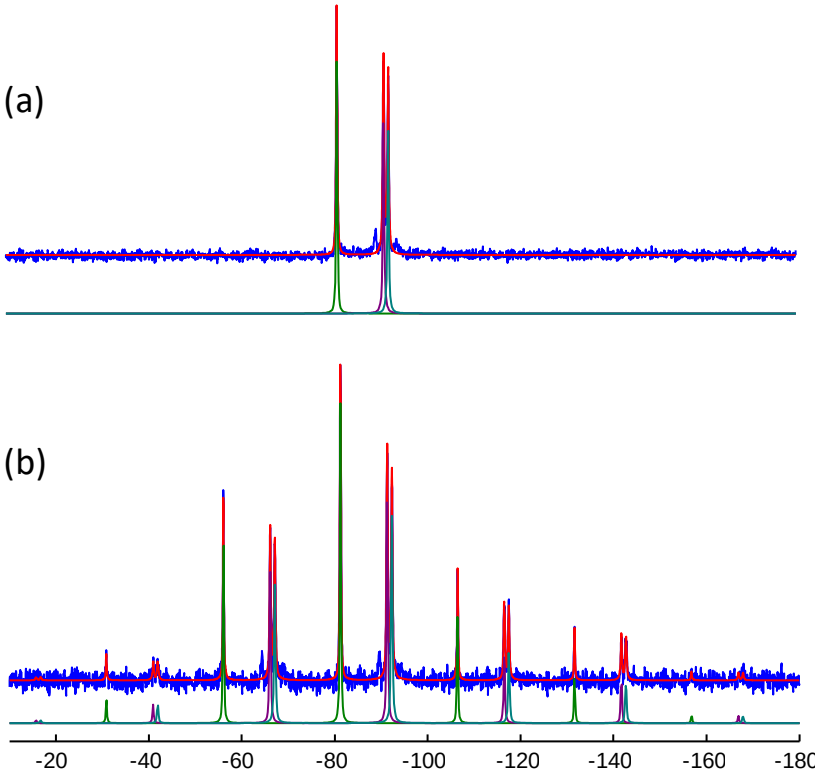

***Figure E3**: Experimental ^{29}Si MAS NMR spectra of the $Ba_2Si_3O_8$ sample (blue) recorded at spinning rates of (a) 10 and (b) 2 kHz, and their simulations (red line). The three contributions corresponding to the three inequivalent Si sites are shown below the spectra.*

***Table E1**: ^{29}Si isotropic chemical shifts (δ_{iso}), chemical shift anisotropy parameters (δ_{csa}, η_{csa}) and relative intensities (I) of the 3 inequivalent Si sites of $Ba_2Si_3O_8$ determined from fits of experimental MAS spectra recorded at 9.4 T with spinning frequencies of 10 and 2 kHz. The ^{29}Si chemical shielding parameters (σ_{iso}, δ_{csa}=-σ_{csa}, η_{csa}) calculated using the GIPAW method for the $Ba_2Si_3O_8$ structure[22] after DFT relaxation of atomic positions are given in italics. Calculated isotropic shifts are obtained from the relationship δ_{iso}=0.939σ_{iso} + 300.5.*

Site	Type		δ_{iso} (ppm)	σ_{iso} (ppm)	δ_{csa} (ppm)	η_{csa}	Fwhm (ppm)	I (%)
Si1	Q^2	Exp	-81.2		-56.5	0.49	0.29	35.1
		GIPAW	*-80.4*	*405.7*	*-60.8*	*0.39*		*33.3*
Si2	Q^3	Exp	-91.3		-59.5	0.28	0.33	33.7
		GIPAW	*-90.7*	*416.6*	*-64.8*	*0.13*		*33.3*
Si3	Q^3	Exp	-92.3		-60.1	0.35	0.33	31.1
		GIPAW	*-91.3*	*417.2*	*-64.6*	*0.16*		*33.3*

F. References

1 C. Collins, M. S. Dyer, M. J. Pitcher, G. F. S. Whitehead, M. Zanella, P. Mandal, J. B. Claridge, G. R. Darling and M. J. Rosseinsky, *Nature*, 2017, **546**, 280–284.
2 C. Collins, G. R. Darling and M. J. Rosseinsky, *Faraday Discuss.*, 2018, **211**, 117–131.
3 C. M. Collins, FUSE, github.com/lrcfmd/FUSE-stable.
4 J. D. Gale and A. L. Rohl, *Mol. Simul.*, 2003, **29**, 291–341.
5 G. Kresse and J. Furthmüller, *Phys. Rev. B*, 1996, **54**, 11169–11186.
6 J. P. Perdew, K. Burke and M. Ernzerhof, *Phys. Rev. Lett.*, 1996, **77**, 3865–3868.
7 G. Kresse and D. Joubert, *Phys. Rev. B*, 1999, **59**, 1758.
8 C. M. Collins, L. M. Daniels, Q. Gibson, M. W. Gaultois, M. Moran, R. Feetham, M. J. Pitcher, M. S. Dyer, C. Delacotte, M. Zanella, C. A. Murray, G. Glodan, O. Pérez, D. Pelloquin, T. D. Manning, J. Alaria, G. R. Darling, J. B. Claridge and M. J. Rosseinsky, *Angew. Chem., Int. Ed.*, 2021, **60**, 16457–16465.
9 S. P. Ong, W. D. Richards, A. Jain, G. Hautier, M. Kocher, S. Cholia, D. Gunter, V. L. Chevrier, K. A. Persson and G. Ceder, *Comp. Mater. Sci.*, 2013, **68**, 314–319.
10 B. Vanbeest, G. Kramer and R. Vansanten, *Phys. Rev. Lett.*, 1990, **64**, 1955–1958.
11 P. S. Baram and S. C. Parker, *Philos. Mag. B-Phys. Condens. Matter Stat. Mech. Electron. Opt. Magn. Prop.*, 1996, **73**, 49–58.
12 M. J. Sanders, M. Leslie and C. R. A. Catlow, *J. Chem. Soc., Chem. Commun.*, 1984, 1271–1273.
13 S. Woodley, https://www.ucl.ac.uk/klmc/Potentials/.
14 A. A. Coelho, *J. Appl. Crystallogr.*, 2018, **51**, 210–218.
15 D. Massiot, F. Fayon, M. Capron, I. King, S. Le Calvé, B. Alonso, J.-O. Durand, B. Bujoli, Z. Gan and G. Hoatson, *Magnetic Resonance in Chemistry*, 2002, **40**, 70–76.
16 C. J. Pickard and F. Mauri, *Physical Review B*, 2001, **63**, 245101.
17 S. J. Clark, M. D. Segall, C. J. Pickard, P. J. Hasnip, M. I. J. Probert, K. Refson and M. C. Payne, *Zeitschrift fur Kristallographie*, 2005, **220**, 567–570.
18 J. R. Yates, C. J. Pickard and F. Mauri, *Physical Review B*, 2007, **76**, 24401.
19 W. Wisniewski, A. J. Fernández-Carrión, P. Schöppe, C. Rüssel and M. Allix, *CrystEngComm*, 2018, **20**, 3455–3466.
20 A. A. Coelho, *J. Appl. Crystallogr.*, 2003, **36**, 86–95.
21 V. Favre-Nicolin and R. Černy, *J. Appl. Cryst*, 2002, **35**, 734–743.
22 K. F. Hesse and F. Liebau, *Z. Kristallogr. - New Cryst. Struct.*, 1980, **153**, 3–17.